

Effects of Dust Evolution on the Vertical Shear Instability in the Outer Regions of Protoplanetary Disks

YUYA FUKUHARA,¹ SATOSHI OKUZUMI,¹ AND TOMOHIRO ONO¹

¹*Department of Earth and Planetary Sciences, Tokyo Institute of Technology, Meguro, Tokyo 152-8551, Japan*

Submitted to ApJ

ABSTRACT

The vertical shear instability (VSI) is a hydrodynamical instability that requires rapid gas cooling and has been suggested to operate in outer regions of protoplanetary disks. The VSI drives turbulence with strong vertical motions, which could regulate the dust growth and settling. However, dust growth and settling can regulate the VSI because dust depletion makes gas cooling inefficient in outer disk regions that are optically thin to their own thermal emission. In this study, we quantify this potentially stabilizing effects of dust evolution on the VSI based on the linear analysis. We construct a model for calculating the cooling timescale, taking into account dust growth beyond micron sizes and size-dependent settling. Combining the model with the linear stability analysis, we map the region where the VSI operates, which we call the VSI zone, and estimate the maximum growth rate at each radial position. We find that dust growth as well as settling makes the VSI zone more confined around the midplane. This causes a decrease in the growth rate because the vertical shear of the rotation velocity, which is the source of the instability, is weaker at lower altitude. In our default disk model with 0.01 solar masses, dust growth from 10 μm to 1 mm causes a decrease in the growth rate by a factor of more than 10. The suppression of VSI-driven turbulence by dust evolution may promote further dust evolution in the outer regions and also explain a high degree of dust settling observed in the disk around HL Tau.

Keywords: protoplanetary disks — hydrodynamics — instabilities

1. INTRODUCTION

Planet formation begins with the evolution of dust grains in protoplanetary disks into kilometer-sized planetesimals. This first stage is initially driven by the growth of dust grains through mutual sticking and condensation (Chokshi et al. 1993; Dominik & Tielens 1997). Large dust particles settle to the midplane and may experience the streaming instability (Youdin & Goodman 2005; Johansen & Youdin 2007) and gravitational instabilities (Goldreich & Ward 1973; Youdin 2011; Takahashi & Inutsuka 2014; Tominaga et al. 2018, 2019, 2020; Pierens 2021), which concentrate the dust particles in a runaway fashion and thereby form planetesimals (e.g., Johansen et al. 2009; Carrera et al. 2015; Yang et al. 2017). The dust particles may also grow directly into planetesimals if the particles are sticky enough (e.g., Okuzumi et al. 2012; Windmark et al. 2012; Kataoka et al. 2013).

Dust evolution in protoplanetary disks depends on gas disk turbulence in many ways. Turbulence enhances the rela-

tive velocity of solid aggregates and may prevent them from sticking together through collisions (e.g., Brauer et al. 2008; Okuzumi & Hirose 2012). Turbulence may also inhibit dust settling toward the disk midplane and formation of a dense dust layer at the midplane (e.g., Dubrulle et al. 1995). Therefore, constraining the level of turbulence in real protoplanetary disks is essential for fully understanding how the dust in the disks evolves into planetesimals.

Recent radio interferometric observations with the Atacama Large Millimeter-submillimeter Array have provided us detailed information of dust evolution and gas turbulence in the outer part of protoplanetary disks. The observations have provided us with ample evidence that massive and large disks commonly have rings and gaps of dust (e.g., ALMA Partnership et al. 2015; Andrews et al. 2018; Long et al. 2018; van der Marel et al. 2019). Although there are a number of potential mechanisms that provide such substructures (for a review, see Andrews 2020), many of them assume that the dust particles comprising the rings have already grown to 0.1–10 mm in size so that they can concentrate radially under the influence of gas drag. Furthermore, the well separated morphology of the dust rings in the disk around HL Tau

(ALMA Partnership et al. 2015) indicates that the dust particles comprising the rings have already settled significantly, with a dust scale height being ten times smaller than the gas scale height (Pinte et al. 2016). Assuming that the dust rings are indeed dominated by millimeter-sized particles, the high degree of settling also points to a low level of turbulence near the midplane. Molecular line emission observations suggest that turbulence in the upper layers of the outer disk regions is also weak (Flaherty et al. 2015, 2017, 2018, 2020).

The absence of strong turbulence in the outer disk regions is consistent with the theoretical expectation that the magnetorotational instability (MRI, Balbus & Hawley 1991) in the outer regions is suppressed by ambipolar diffusion (Simon et al. 2013a,b; Bai 2015; Riols & Lesur 2018). However, the suppression of the MRI is not enough to explain the absence of strong turbulence because purely hydrodynamic disk instabilities can also drive turbulence (for a review, see Lyra & Umurhan 2019). Among them, the most robust one in outer regions of protoplanetary disks is the vertical shear instability (VSI, Urpin & Brandenburg 1998; Nelson et al. 2013; Lin & Youdin 2015). The VSI is an instability caused by a vertical gradient in the gas rotation velocity together with a cooling timescale much shorter than the orbital timescale (Urpin 2003; Nelson et al. 2013; Lin & Youdin 2015). The requirement of rapid gas cooling tends to be met in outer disk regions where the optical depth is low (Malygin et al. 2017; Pfeil & Klahr 2019). Once the VSI operates, it produces turbulence with predominant vertical motion (e.g., Stoll & Kley 2014), which would efficiently prevent vertical dust settling (Flock et al. 2017, 2020).

The question then is what can suppress the VSI in outer regions of protoplanetary disks. One candidate is strong magnetic field as suggested by Nelson et al. (2013) and Cui & Bai (2020). In this paper, we explore the potential role of dust evolution, i.e., dust growth and settling, in suppressing the VSI. It is natural to expect that dust evolution should affect the VSI as it is the dust that is responsible for disk cooling. Malygin et al. (2017) already noted that a depletion of small grains slows down cooling in disk regions that are optically thin to their own thermal emission. This implies that both dust evolution growth and settling should lead to suppression of the VSI, although no quantitative assessment of the effects has been made so far.

The goal of this study is to clarify the influences of dust growth and settling on the stability of outer (5–100 au) protoplanetary disk regions against the VSI. We calculate the thermal relaxation (cooling) timescale in the outer disk regions using a parametrized dust model in which the maximum particle size and dust vertical diffusion coefficient are given as free parameters. Using the two-dimensional maps of the thermal relaxation timescale together with linear stability analysis, we study how the location of the VSI-active region

and the VSI growth rate in the region vary as dust grows and settles.

This paper is organized as follows. In Section 2, we review the basic properties of the VSI, deriving the linear dispersion relation that gives the growth rate of the VSI at each location in a disk. We then describe our model in Section 3, present the main results in Section 4, and discuss limitations and implications of our study in Section 5. Section 6 presents a summary.

2. THE VSI

In this section, we review the basic properties of the VSI and derive the dispersion relation that is used in the following section. The VSI is a type of the Goldreich–Schubert–Fricke instability (Goldreich & Schubert 1967; Fricke 1968) known in the context of differentially rotating stars. The presence of a vertical gradient in gas angular velocity Ω is one of the necessary conditions for the VSI to operate. The radial and vertical force balances give

$$\Omega^2 = \frac{GM_*}{(R^2 + z^2)^{3/2}} + \frac{1}{R\rho_g} \frac{\partial P}{\partial R}, \quad (1)$$

$$\frac{\partial(R\Omega)}{\partial z} = \frac{1}{2\Omega\rho_g^2} \left(\frac{\partial P}{\partial z} \frac{\partial\rho_g}{\partial R} - \frac{\partial P}{\partial R} \frac{\partial\rho_g}{\partial z} \right), \quad (2)$$

where R is the cylindrical distance from the central star, z is the height from the midplane, M_* is the mass of the central star, P is the gas pressure, ρ_g is the gas density, and G is the gravitational constant. The vertical shear $\partial(R\Omega)/\partial z$ is nonzero if the temperature gradient exists in the radial direction (Urpin 2003, see also Equation (17) in Section 3.1).

2.1. The Thermal Criterion for Instability

However, buoyant forces can stabilize the VSI when the entropy increases in the direction of decreasing gas pressure (Lin & Youdin 2015). The Brunt–Väisälä frequency N_z is given by

$$N_z^2 \equiv -\frac{1}{\rho_g C_p} \cdot \frac{\partial P}{\partial z} \cdot \frac{\partial s}{\partial z}, \quad (3)$$

where C_p and s are the specific heat at constant pressure and the specific entropy, respectively. The specific entropy is given by $s = C_V \log(P/\rho_g^\gamma)$, where C_V is the specific heat at constant volume and γ is the heat capacity ratio. The vertical buoyancy is stabilizing if $N_z^2 > 0$. In protoplanetary disks, the pressure decreases with distance z from the midplane. In outer disk regions where the temperature is determined by stellar irradiation (e.g., Chiang & Goldreich 1997), the entropy increases with z , thus stabilizing the VSI.

Therefore, the VSI requires fast thermal relaxation that reduces buoyancy (Nelson et al. 2013). This requirement can be expressed as

$$\tau_{\text{relax}} \lesssim \tau_{\text{crit}}. \quad (4)$$

Here, τ_{crit} is the critical thermal relaxation timescale defined by (Lin & Youdin 2015)

$$\tau_{\text{crit}} = \frac{H_g}{R} \frac{|q|}{\gamma - 1} \Omega_K^{-1}, \quad (5)$$

where Ω_K is the Keplerian frequency, H_g is the gas scale height, and q is the radial gradient of the temperature. Strictly speaking, high- k_x unstable modes persist for $\tau_{\text{relax}} \gtrsim \tau_{\text{crit}}$, but we neglect these modes because their growth rates are much smaller than the maximum growth rates for $\tau_{\text{relax}} \lesssim \tau_{\text{crit}}$. We describe more details of the thermal relaxation timescale τ_{relax} in Section 3.2.1.

In realistic protoplanetary disks, Equation (4) is fulfilled in regions around the midplane (Malygin et al. 2017; Pfeil & Klahr 2019, see also Section 4 of this paper). In this study, we refer to such a region as a VSI zone.

2.2. Linear Analysis

A number of previous studies already derived dispersion relations with and without gas cooling and vertical stratification (Urpin & Brandenburg 1998; Urpin 2003; Arlt & Urpin 2004; Nelson et al. 2013; Barker & Latter 2015; Lin & Youdin 2015, 2017; Latter & Papaloizou 2018). Here, we follow Nelson et al. (2013, 2016) and derive a local dispersion relation.

We consider a VSI zone with the finite vertical extent and focus on linear modes whose wavelengths are short enough to fit into the zone (see Section 3.2.2 for the allowed range of wavenumbers). We apply a locally isothermal equation of state to the VSI zone and regard the modes within the zone as radially and vertically local. We note that Lin & Youdin (2015) presents a dispersion relation for vertically global VSI modes including the effect of finite thermal relaxation. However, we do not use this here because it is not strictly applicable to disks with vertically varying τ_{relax} .

Under the local shearing box approximation, the equation of continuity can be written as

$$\frac{\partial \rho_g}{\partial t} + \nabla \cdot (\rho_g v) = 0, \quad (6)$$

where ρ_g is the gas density and $v = (v_x, v_y, v_z)$ is the gas velocity with three components for the radial, azimuthal and vertical velocities in the Cartesian shearing box. The equations of motion of gas in the shearing box are

$$\frac{\partial v_x}{\partial t} + (v \cdot \nabla) v_x = -\frac{1}{\rho_g} \frac{\partial P}{\partial x} + 2\Omega_0 v_y + 3\Omega_0^2 x, \quad (7)$$

$$\frac{\partial v_y}{\partial t} + (v \cdot \nabla) v_y = -\frac{1}{\rho_g} \frac{\partial P}{\partial y} - 2\Omega_0 v_x, \quad (8)$$

$$\frac{\partial v_z}{\partial t} + (v \cdot \nabla) v_z = -\frac{1}{\rho_g} \frac{\partial P}{\partial z} - g, \quad (9)$$

where $\Omega_0 = \text{constant}$ is the angular velocity in the shearing box, and $g = \Omega_0^2 z$ is the vertical component of stellar gravity. Following Goldreich & Schubert (1967), we consider the vicinity of a given height $z = z_0$ and assume that g and the isothermal sound speed $c_s = \sqrt{P/\rho_g}$ are approximately constant on this small vertical scale.

We assume axisymmetry and consider perturbations of the form $\propto e^{-i\omega t + ik_x x + i(k_z - ig/(2c_s^2))z}$ on the steady background. Here, ω is the angular frequency and k_x and k_z are the radial and vertical wavenumbers, respectively. The factor $e^{gz/(2c_s^2)}$ accounts for the variation of the background density in the vertical direction (Nelson et al. 2013). The dispersion relation for the perturbations is (see Nelson et al. (2013) and Nelson et al. (2016) for a derivation)

$$\omega^4 - \left[c_s^2 (k_x^2 + k_z^2) + \kappa_0^2 + \frac{g^2}{4c_s^2} \right] \omega^2 - 2\Omega_0 c_s^2 k_x k_z \frac{\partial v_{y0}}{\partial z} + i\Omega_0 g k_x \frac{\partial v_{y0}}{\partial z} + \kappa_0^2 \left(c_s^2 k_z^2 + \frac{g^2}{4c_s^2} \right) = 0, \quad (10)$$

where v_{y0} and κ_0 are the rotation velocity deviation and epicyclic frequency, respectively, for the background; the latter one can be written as

$$\kappa_0^2 = 2\Omega_0 \left(\frac{\partial v_{y0}}{\partial x} + 2\Omega_0 \right). \quad (11)$$

For an unstable perturbation that satisfies Equation (10), the growth rate is given by

$$\Gamma_{\text{VSI}} = \text{Im}(\omega). \quad (12)$$

3. MODEL

We study the VSI linear stability of protoplanetary disks taking into account dust growth and settling. We present a gas disk model in Section 3.1, a model for calculating the disk relaxation time and VSI growth rate in Section 3.2, a dust model used to calculate the thermal relaxation time in Section 3.3, and our parameter choice in Section 3.4.

3.1. Gas Disk Model

We consider an axisymmetric disk around a solar-mass star. The gas surface density is given by

$$\Sigma_g(R) = \frac{(2 - \beta_\Sigma) M_{\text{disk}}}{2\pi R_c^2} \left(\frac{R}{R_c} \right)^{-\beta_\Sigma} \exp \left[-\left(\frac{R}{R_c} \right)^{2-\beta_\Sigma} \right], \quad (13)$$

where M_{disk} is the total mass of the gas disk, R_c is the characteristic radius, and β_Σ is a dimensionless number characterizing the radial slope of the gas surface density. Equation (13) is motivated by the similarity solution of the viscous accretion disk model (Lynden-Bell & Pringle 1974; Hartmann

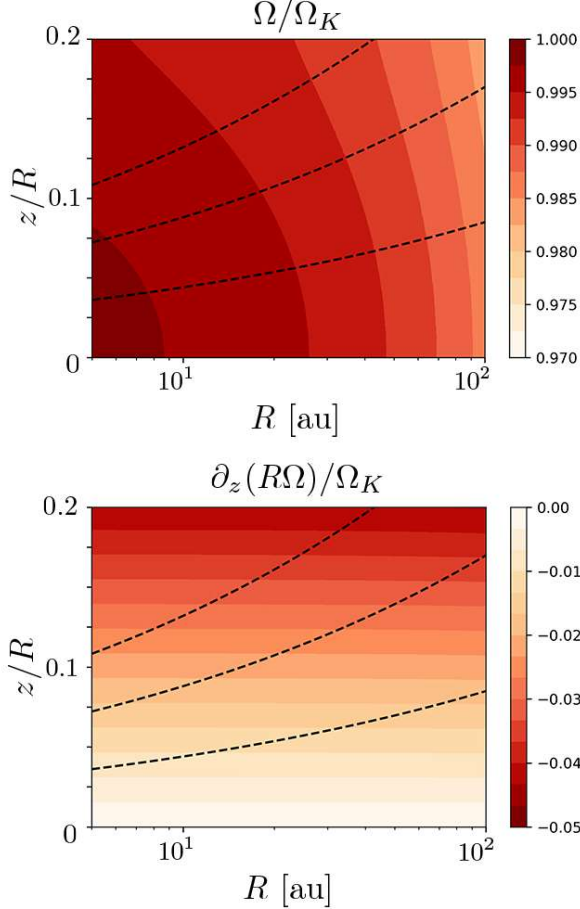


Figure 1. Local rotational angular velocity Ω (upper panel) and vertical shear $\partial(R\Omega)/\partial z$ (lower panel), as a function of R and z/R . The dashed lines represent H_g , $2H_g$, and $3H_g$ in height from the midplane.

et al. 1998) although we do not consider disk evolution in this study. Since we are primarily interested in the effects of dust growth and settling on the VSI, we fix the gas disk parameters to $M_{\text{disk}} = 0.01M_{\odot}$, $R_c = 100$ au, and $\beta_{\Sigma} = 1$ except in Section 4.3, where we show that disks of higher disk dust masses have more extended VSI zones. The heat capacity ratio γ and mean molecular mass m_g of the gas is taken to be 1.4 and $2.3m_p$, respectively, where m_p is the proton mass.

We focus on the outer region of the disk where the temperature is determined by stellar irradiation. Assuming that the disk is optically thick to stellar radiation¹ and that the stellar luminosity is equal to the solar luminosity, the temperature

¹ A disk region that is optically thin to its own thermal emission can be optically thick to the radiation from the central star because the opacity in the visible is higher than that in the infrared and, more importantly, because the radial optical depth is $\sim R/H_g$ (~ 10 – 100) times larger than the vertical optical depth (Chiang & Goldreich 1997).

of the disk interior is given by

$$T(R) = 130 \left(\frac{R}{1 \text{ au}} \right)^q \text{ K} \quad (14)$$

with $q = -3/7$ (Chiang & Goldreich 1997). Viscous heating is negligible as long as we focus on $R \gtrsim 10$ au (e.g., Bitsch et al. 2015). We assume that the disk interior is vertically isothermal, neglecting warmer surface layers that are optically thin to the starlight (Chiang & Goldreich 1997).

From vertical hydrostatic equilibrium, the gas density is given by

$$\rho_g(R, z) = \frac{\Sigma_g}{\sqrt{2\pi}H_g} \exp\left(-\frac{z^2}{2H_g^2}\right) \quad (15)$$

with $H_g = c_s/\Omega_K$, $\Omega_K = \sqrt{GM_*/R^3}$, and $M_* = 1M_{\odot}$.

The vertical shear of the gas rotation velocity, $\partial v_{\phi 0}/\partial z = \partial(R\Omega)/\partial z$, characterizes the strength of the VSI. Because we assume a radially varying temperature profile, $\partial(R\Omega)/\partial z$ is nonzero at all height except at the midplane. This can be analytically shown for $R \ll R_c$, where $\Sigma_g \propto R^{-\beta_{\Sigma}}$. In this region, Ω and $\partial(R\Omega)/\partial z$ can be approximated as (Takeuchi & Lin 2002)

$$\Omega(R, z) \approx \Omega_K \left[1 + \frac{1}{2} \left(\frac{H_g}{R} \right)^2 \left(-\beta_{\Sigma} + \frac{q-3}{2} + \frac{q}{2} \frac{z^2}{H_g^2} \right) \right], \quad (16)$$

and

$$\frac{\partial(R\Omega)}{\partial z} \approx \frac{q}{2} \frac{z}{R} \Omega_K, \quad (17)$$

respectively. Equation (17) proves that a nonzero radial temperature gradient is the source of the vertical shear (e.g., Lin & Youdin 2015). Figure 1 shows the gas angular velocity $\Omega(R, z)$ and the vertical shear of the angular velocity $\partial(R\Omega)/\partial z$ in the disk, including the region $R \gtrsim R_c$. From the lower panel of Figure 1, and also from Equation (17), the vertical shear increases with z , suggesting that the VSI is stronger at higher altitude as long as the cooling criterion (Equation (4)) is fulfilled.

We assume that the disk is weakly turbulent and express the turbulent diffusion coefficient as $\alpha_D c_s H_g$, where α_D is the dimensionless parameter characterizing the level of turbulent diffusion. Turbulent diffusion controls the maximum wavenumber of the VSI modes (Section 3.2.2) and the vertical scale height of dust particles (Section 3.3). In principle, α_D in outer disk regions should depend on the strength of VSI-driven turbulence, and hence on the VSI growth rate Γ_{VSI} , which is the output of our model. Therefore, a self-consistent determination of α_D and Γ_{VSI} requires a model that predicts the former as a function of the latter. Lacking such a model, we opt for taking α_D as a free parameter, although we do discuss potential feedback of dust settling on the level of VSI-driven turbulence in Section 5.2.

3.2. Instability Analysis

We analyze the linear stability of the model disk against the VSI in the following three steps. In the first step, we use the thermal relaxation criterion (Equation (4)) to search for the disk region, which we call the VSI zone, where the linear VSI operates (Section 3.2.1). In the second step, we compute the range of wavenumbers for the VSI modes that fit into the active zone (Section 3.2.2). In the third step, we calculate the maximum growth rate of the VSI at each radial location (Section 3.2.3).

3.2.1. Defining the VSI Zone

We compute the radial and vertical extent of the VSI zone by applying the thermal relaxation criterion (Equation (4)) to each point (R, z) in the disk. In protoplanetary disks, local thermal relaxation is regulated either by collisional heat transfer from gas to dust or by radiative cooling (Malygin et al. 2017). The area around the boundary of the VSI zone can be regarded as optically thin (Malygin et al. 2017). Following Malygin et al. (2017) and Pfeil & Klahr (2019), we estimate the local thermal relaxation timescale τ_{relax} as

$$\tau_{\text{relax}} = \max(\tau_{\text{coll}}, \tau_{\text{emit}}), \quad (18)$$

where τ_{coll} and τ_{emit} are the timescales of collisional heat transfer and radiative cooling, respectively.

The timescale of collisional heat transfer is given by

$$\tau_{\text{coll}} = \frac{\ell_{\text{gd}}}{v_{\text{th}}}, \quad (19)$$

where ℓ_{gd} is the mean travel length of gas molecules before colliding with dust particles and v_{th} is the mean relative velocity between the gas molecules and dust particles. The relative velocity v_{th} can be approximated as the mean thermal speed of the molecules,

$$v_{\text{th}} \approx \sqrt{\frac{8k_{\text{B}}T}{\pi m_{\text{g}}}}, \quad (20)$$

where k_{B} is the Boltzmann constant. The radiative cooling timescale τ_{emit} in the optically thin limit is given by (Malygin et al. 2017)

$$\tau_{\text{emit}} = \frac{C_{\text{V}}}{16\kappa_{\text{P}}(T)\sigma_{\text{SB}}T^3}, \quad (21)$$

where $\kappa_{\text{P}}(T)$ is the Planck mean opacity per unit gas mass and σ_{SB} is the Stefan–Boltzmann constant. Both ℓ_{gd} and κ_{P} depend on the local size distribution of the dust particles. Our dust model is described in Section 3.3.

In general, collisional heat transfer regulates the cooling timescale at high altitude where the dust density is low (Malygin et al. 2017). Because the dust density decreases monotonically with $|z|$, there is the height $|z| = L$ above which the VSI is stable. In other words, the VSI zone refers to the region where $|z| < L$. Note that L generally depends on R and becomes zero where the VSI is stable at all heights.

3.2.2. Wavenumber Range of the VSI Modes

The VSI modes generally have $k_x k_z < 0$ (Arlt & Urpin 2004), so we restrict $k_x > 0$ and $k_z < 0$. Below we further restrict the wavelength range permitted for VSI modes by accounting for viscous damping and the finite thickness of the VSI zone.

Viscous damping erases unstable modes of short wavelengths, giving upper limits on k_x and $|k_z|$ for the true VSI modes. We particularly focus on the upper limit on the radial wavenumbers because VSI modes typical have $k_x \gg |k_z|$ (Arlt & Urpin 2004). The maximum wavenumber set by viscous damping can be estimated as (Lin & Youdin 2015)

$$(k_{x,\text{max}} H_{\text{g}})^2 \approx \frac{|q| H_{\text{g}}}{\alpha_{\text{D}} R} \quad (22)$$

or equivalently,

$$k_{x,\text{max}} \approx \sqrt{\frac{|q|}{\alpha_{\text{D}} R H_{\text{g}}}}. \quad (23)$$

Because the VSI zone has a finite vertical extent, only modes whose vertical wavelengths are short enough to “fit” into the zone can be unstable. Specifically, we require the VSI modes at each R to have half wavelengths shorter than the vertical zone width $2L$. In other words, the vertical wavenumbers of the VSI modes must satisfy $|k_z| > |k_z|_{\text{min}}$, where

$$|k_z|_{\text{min}} \approx \frac{\pi}{2L}. \quad (24)$$

3.2.3. The Maximum Growth Rate

The local dispersion relation (Equation (10)) formally gives the growth rate of the VSI at each (R, z) . However, the most unstable VSI modes typically have vertical wavelengths comparable to H_{g} (e.g., Nelson et al. 2013, see also Section 4.2). Physically, such long-wavelength modes should be regarded as extending over the whole vertical extent of the VSI zone.

For this reason, we opt for a semi-local approach in which we calculate the maximum VSI growth rate $\Gamma_{\text{VSI,max}}$ at each R using the linear dispersion relation, but limiting the range of vertical wavenumbers to $|k_z| \geq |k_z|_{\text{min}}$ to account for the finite vertical extent of the VSI zone. The vertically local quantities $g(= -\Omega_{\text{K}}^2 z)$ and $v_{y0}(= R\Omega(R, z))$ involved in the local dispersion relation are evaluated at the vertical boundary of the VSI zone, $|z| = L$, because the VSI is generally more vigorous at higher altitude unless buoyancy suppresses it (Nelson et al. 2013). We also limit radial wavenumbers to $k_x \leq k_{x,\text{max}}$ to account for viscous damping.

Besides, the local analysis in this study and the vertically global analysis by Lin & Youdin (2015) give similar predictions for the body mode in a vertically wide VSI zone (see Section 5.1).

3.3. Dust Model

We here describe the dust model we use to calculate ℓ_{dg} and κ_{P} . We consider spherical, icy dust particles of internal density $\rho_{\text{int}} = 1 \text{ g cm}^{-3}$. The ratio between the dust surface density Σ_d and Σ_g is fixed to the interstellar dust abundance of 1%, whereas the local dust-to-gas ratio is allowed to vary with z considering dust settling. As we discuss in Section 4.3, the VSI zone shrinks as Σ_d decreases.

The particle size distribution is assumed to follow a power law

$$\frac{dN_d(a)}{da} = \begin{cases} \frac{3\Sigma_d}{8\pi\rho_{\text{int}}(\sqrt{a_{\text{max}}}-\sqrt{a_{\text{min}}})} a^{-7/2}, & a_{\text{min}} < a < a_{\text{max}}, \\ 0, & \text{otherwise,} \end{cases} \quad (25)$$

where $dN_d(a)/da$ is the number surface density per unit particle size a , Σ_d is the total dust mass surface density, and a_{min} and a_{max} are the minimum and maximum particle sizes, respectively. The size distribution given by Equation (25) satisfies the normalization

$$\Sigma_d = \int_{a_{\text{min}}}^{a_{\text{max}}} m \frac{dN_d(a)}{da} da, \quad (26)$$

where $m = (4\pi/3)\rho_{\text{int}}a^3$ is the particle mass. The power-law slope assumed in Equation (25) is simply taken from the interstellar particle size distribution (Mathis et al. 1977). We note, however, that the size distribution can be somewhat shallower or steeper than assumed in Equation (25) depending on the details of collisional growth and fragmentation (Birnstiel et al. 2011).

We take the maximum particle size a_{max} as a free parameter to study the impact of dust growth on the VSI. The minimum particle size is less well defined, but we may crudely taken it to be $\sim 0.1\text{--}1 \mu\text{m}$ because particles smaller than these sizes grow quickly through Brownian motion (Birnstiel et al. 2011). We fix $a_{\text{min}} = 1 \mu\text{m}$ throughout this study.

Assuming the balance between settling and diffusion, the vertical distribution of the particles can be written as (Takeuchi & Lin 2002)

$$\frac{dn_d(a, z)}{da} = C_d(a) \exp\left[-\frac{z^2}{2H_g^2} - \frac{\text{St}_{\text{mid}}}{\alpha_D} \left(\exp\frac{z^2}{2H_g^2} - 1\right)\right], \quad (27)$$

where $dn_d(a, z)/da$ is the particle number density per unit radius at height z , St_{mid} is the Stokes number of the particles at the midplane, and $C_d(a)$ is the normalized constant determined by the condition

$$\frac{dN_d(a)}{da} = \int \frac{dn_d(a, z)}{da} dz. \quad (28)$$

The Stokes number is the product of the stopping time and Keplerian frequency. Assuming that the particle radius are smaller than the mean free path of the disk gas molecules,

gas drag onto the particles follows Epstein's law, which gives (see, e.g., Birnstiel et al. 2010)

$$\text{St}_{\text{mid}} = \frac{\pi\rho_{\text{int}}a}{2\Sigma_g}. \quad (29)$$

To evaluate C_d , we note that the integral in Equation (28) is dominated by the region $z \lesssim H_g$, for which the Equation (27) can be approximated as $dn_d(a, z)/da \approx C_d(a) \exp(-z^2/(2H_g^2))$, where

$$H_d = \left(1 + \frac{\text{St}_{\text{mid}}}{\alpha_D}\right)^{-1/2} H_g \quad (30)$$

represents the scale height of particles with size a (Dubrulle et al. 1995; Youdin & Lithwick 2007). This approximation gives

$$C_d(a) = \frac{1}{\sqrt{2\pi}H_d} \frac{dN_d(a)}{da}. \quad (31)$$

The vertical-size distribution $dn_d(a, z)/da$ gives ℓ_{gd} and κ_{P} as a function of z . The mean travel length of gas molecules colliding with dust particles ℓ_{gd} is given by

$$\ell_{\text{gd}} = \left(\int_{a_{\text{min}}}^{a_{\text{max}}} \pi a^2 \frac{dn_d}{da} da\right)^{-1}. \quad (32)$$

The Planck mean opacity κ_{P} per unit gas mass can be written as

$$\kappa_{\text{P}}(T) = \frac{1}{\rho_g} \int_{a_{\text{min}}}^{a_{\text{max}}} \sigma_{\text{abs,P}}(a, T) \frac{dn_d}{da} da, \quad (33)$$

where $\sigma_{\text{abs,P}}(a, T)$ is the Planck mean absorption cross section of the particles. In this study, we approximate $\sigma_{\text{abs,P}}$ with the monochromatic absorption cross section $\sigma_{\text{abs}}(a, \lambda)$ at wavelength $\lambda = \lambda_{\text{peak}}(T)$, where

$$\lambda_{\text{peak}}(T) = 10 \mu\text{m} \left(\frac{300 \text{ K}}{T}\right) \quad (34)$$

is the peak wavelength of the Planck function. Furthermore, we crudely approximate $\sigma_{\text{abs}}(a, \lambda)$ as

$$\sigma_{\text{abs}}(a, \lambda) = \pi a^2 \min\left(1, \frac{2\pi a}{\lambda}\right), \quad (35)$$

where the factor $2\pi a/\lambda$ is called the size parameter in Mie scattering theory (see, e.g., Bohren & Huffman 1983). This approximate expression satisfies the asymptotic properties of Mie scattering that σ_{abs} approaches the geometric cross section πa^2 in the short wavelength limit ($\lambda \ll 2\pi a$) and that the dust mass opacity σ_{abs}/m is independent of a in the long wavelength limit ($\lambda \gg 2\pi a$).

We neglect the radial inward drift of the dust particles due to gas drag (Whipple 1972; Adachi et al. 1976; Weidenschilling 1977) and assume that the dust surface density profile is constant in time. This approach is valid if the

VSI growth timescale is shorter than the dust drift timescale. For $St_{\text{mid}} < 1$, which is the case for the dust particles considered in our model, the drift timescale can be estimated as $\sim (R/H_g)^2 St_{\text{mid}}^{-1} \Omega_K^{-1}$ (see the references listed above). In the limit of short relaxation timescales, the VSI grows on a timescale of $\sim (R/H_g) \Omega_K^{-1}$ (e.g., [Urpin & Brandenburg 1998](#); [Nelson et al. 2013](#)), which is shorter than the drift timescale as long as $St_{\text{mid}} < 1$. However, radial dust drift may not be negligible when a finite relaxation time suppresses the growth of the VSI. In this case, dust depletion due to the radial inward drift would further suppress the VSI as we demonstrate in Section 4.3.

3.4. Computational Domain and Parameter Choices

We consider a disk region defined by $5 \text{ au} < R < 100 \text{ au}$ and $0 < z/R < 0.2$ and divide the region into 1000 logarithmically spaced radial grids and 1000 linearly spaced vertical grids. The dust size distribution is divided into logarithmic bins of 10 grids per decade in a . The main free parameters in our model are the vertical diffusion coefficient α_D and maximum dust particle size a_{max} . We take $\alpha_D = 10^{-3}, 10^{-4}$, and 10^{-5} and $a_{\text{max}} = 10 \mu\text{m}, 100 \mu\text{m}$, and 1 mm .

4. RESULTS

In this section, we use the model presented in Section 3 to study how dust growth and settling affects the VSI stability of protoplanetary disks. We map the VSI zones in Section 4.1 and then compute the radial distribution of the growth rate and wavenumbers of the most unstable VSI model in Section 4.2. We study the dependence of the VSI zone size on the dust and gas surface densities in Section 4.3.

4.1. Radial and Vertical Extent of the VSI Zone

As described in Section 2, the VSI is active where the thermal relaxation time τ_{relax} (Equation (18)) is shorter than the critical timescale τ_{crit} (Equation (5)). We find that τ_{relax} (Equation (18)) is determined by the collisional cooling timescale τ_{coll} for all parameters and all regions explored in this study. Figure 2 plots $\tau_{\text{coll}}/\tau_{\text{emit}}$ and $\tau_{\text{coll}}/\tau_{\text{crit}}$ as a function of R and z for $\alpha_D = 10^{-4}$ and $a_{\text{max}} = 10 \mu\text{m}$, showing that τ_{coll} is about an order-of-magnitude larger than τ_{emit} at all locations. Our result is consistent with that of [Malygin et al. \(2017\)](#), who showed that $\tau_{\text{coll}} > \tau_{\text{emit}}$ in an optically thin region away from the central star (see their Figure 3). The maps of τ_{relax} (in units of Ω_K^{-1}) for all parameter sets are shown in Figures 11 and 12 in Appendix A.

The solid line in the lower panel of Figure 2 indicates the boundary of the the VSI zone; below this line, one has $\tau_{\text{relax}} (= \tau_{\text{coll}}) < \tau_{\text{crit}}$ and the VSI operates.² In this example,

² To be precise, the VSI zone does not include the midplane ($z = 0$), where the vertical shear vanishes.

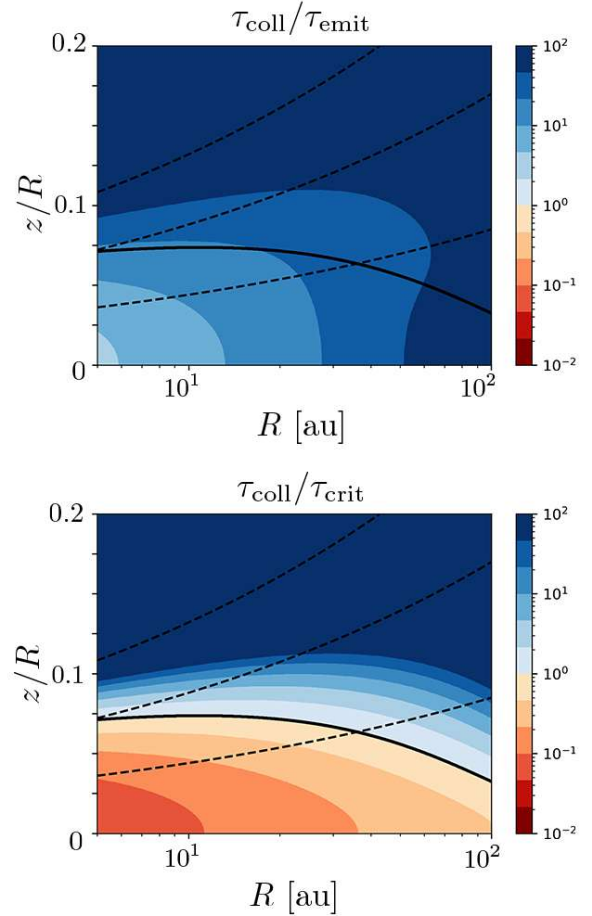


Figure 2. Collisional timescale τ_{coll} normalized by radiative cooling timescale τ_{emit} (upper panel) and critical thermal relaxation timescale τ_{crit} (lower panel) as a function of R and z/R for $\alpha_D = 10^{-4}$ and $a_{\text{max}} = 10 \mu\text{m}$. The thermal relaxation timescale is given by the larger of the two (see Equation (18)). The dashed lines represent $z = H_g, 2H_g$, and $3H_g$. The solid line marks $\tau_{\text{coll}} = \tau_{\text{crit}}$.

the VSI zone extends to $z \sim 0.5-2H_g$ at $5 \text{ au} < R < 30 \text{ au}$. The vertical width of the VSI zone diminishes as R increases. The vertical optical depth from infinity to the VSI zone boundary is $O(1)$ at $R \sim 10 \text{ au}$ and decreases with increasing R , so using the thermal relaxation timescale for the optically thin limit (Section 3.2.1) is marginally justified.

Figure 3 indicates the location of the VSI zone for $a_{\text{max}} = 100 \mu\text{m}$ but with different values of α_D . This figure illustrates how dust settling affects the extent of the VSI zone; in our model, the dust scale height decreases with decreasing α_D (see Equation (30)). We find that dust settling leads to a VSI zone that is more confined to the midplane region and more extended to larger radial distances. This is because the settling causes dust depletion and dust concentration, which increase and decrease the thermal relaxation timescale $\tau_{\text{relax}} = \tau_{\text{coll}} \propto \ell_{\text{gd}}$, at high and low altitude, respec-

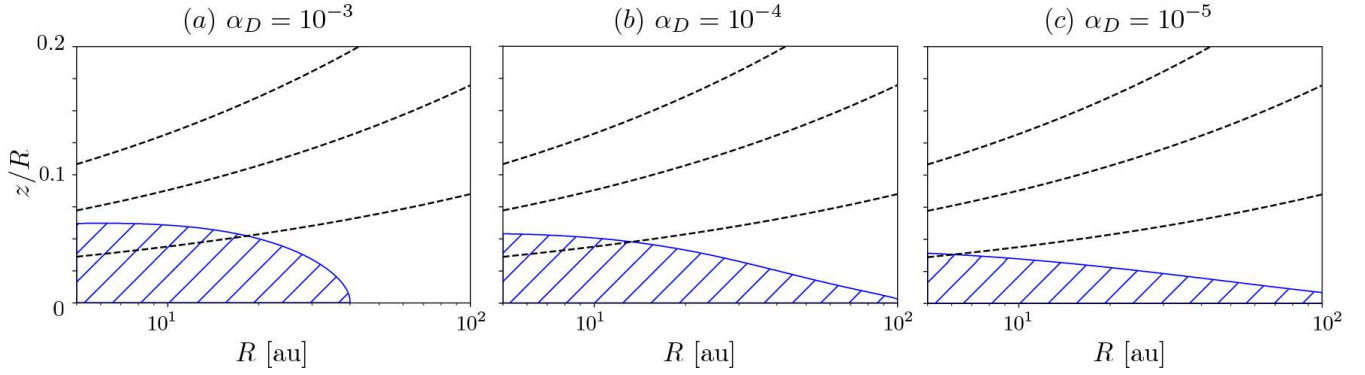


Figure 3. Location of the VSI zone (the shaded area) for different values of α_D with $a_{\max} = 100 \mu\text{m}$. The dashed lines represent H_g , $2H_g$, and $3H_g$ in height from the midplane.

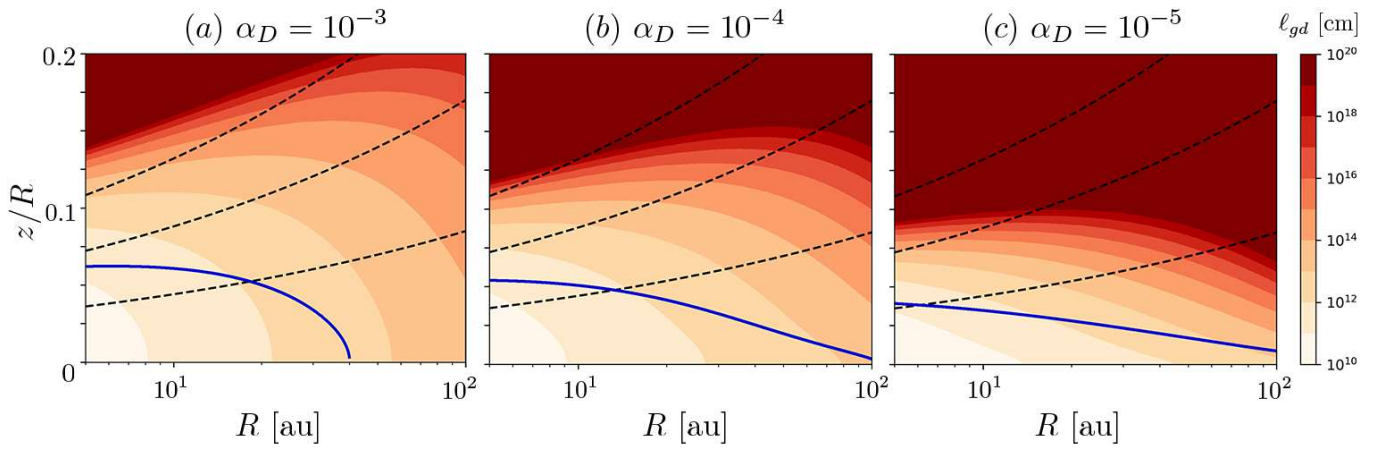


Figure 4. Mean travel length of gas molecules before colliding with dust particles, ℓ_{gd} , as a function of R and z/R for different values of α_D with $a_{\max} = 100 \mu\text{m}$. The dashed lines represent H_g , $2H_g$, and $3H_g$ in height from the midplane. The solid lines correspond to the boundary of the VSI zone.

tively (see also Figure 11). See Figure 4 for the variation of ℓ_{gd} at different locations with α_D .

The stabilizing effect of dust setting on the VSI at the midplane can also be confirmed by looking at how ℓ_{gd} at the midplane depends on α_D . For simplicity, we assume $\alpha_D < \text{St}_{\text{mid}}$, which holds in our model at sufficiently large R ($R \gtrsim 50$ au for $\alpha_D = 10^{-4}$). With this assumption, we approximate $H_d \sim (\alpha_D/\text{St}_{\text{mid}})^{1/2} H_g$ and $dn_d(z=0)/da \propto (\text{St}_{\text{mid}}/\alpha_D)^{1/2} dN_d/da$. Using this, the integration in Equation (32) can be analytically performed, resulting in

$$\ell_{\text{gd}}(z=0) \propto \frac{\Sigma_{\text{g}}^{1/2}}{\Sigma_{\text{d}}} \frac{a_{\max}^{1/2}}{\log(a_{\max})} \alpha_D^{1/2} \quad (36)$$

for $a_{\max} \gg a_{\min}$. Equation (36) confirms that ℓ_{gd} at the midplane decreases with decreasing α_D (see Figure 4).

Figure 5 indicates the location of the VSI zone for different values of a_{\max} , illustrating how the VSI zone evolves with dust growth. The figure shows that the VSI zone shrinks toward the midplane and toward the central star as a_{\max} increases. This is because increasing a_{\max} decreases dust par-

ticles' total surface area and thus increases ℓ_{gd} as shown in Figure 6. In fact, increasing a_{\max} also promotes dust settling, which acts to decrease ℓ_{gd} at the midplane. However, we find that this effect is minor compared to the increase in the midplane ℓ_{gd} due to local dust growth. This can also be confirmed from Equation (36) implying that ℓ_{gd} at the midplane increases with a_{\max} . Well above the midplane, both dust settling and local dust growth increase ℓ_{gd} , stabilizing the VSI. A closer inspection shows that local dust growth dominates the increase of ℓ_{gd} at $z \lesssim 1-2H_g$.

4.2. The Maximum Growth Rate and Wavenumbers

We search for the most unstable VSI mode at each R using the procedure described in Section 3.2.3. For the entire parameter space explored in this study, we find that the most VSI mode always lies at $k_x = k_{x,\max}$ and $|k_z| = |k_{z,\min}|$. This is illustrated in Figure 7, where we plot the VSI growth rate Γ_{VSI} as a function of k_x and k_z at the top of the VSI zone at $R = 60$ au in the case of $a_{\max} = 10 \mu\text{m}$ and $\alpha_D = 10^{-4}$. In this example, we have $k_{x,\max} \approx 18/H_g$ and $|k_{z,\min}| \approx 1.7/H_g$

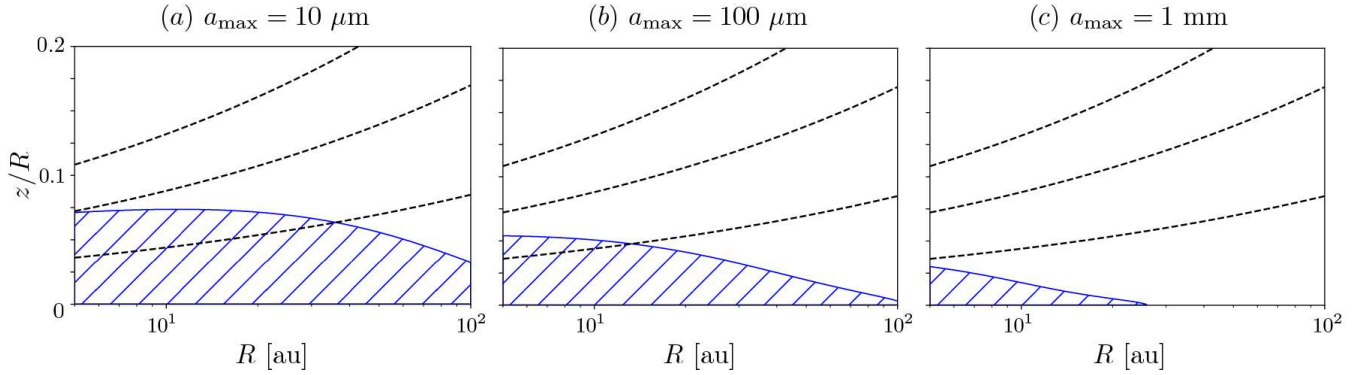


Figure 5. Location of the VSI zone (the shaded area) for different values of a_{\max} with $\alpha_D = 10^{-4}$. The dashed lines represent H_g , $2H_g$, and $3H_g$ in height from the midplane.

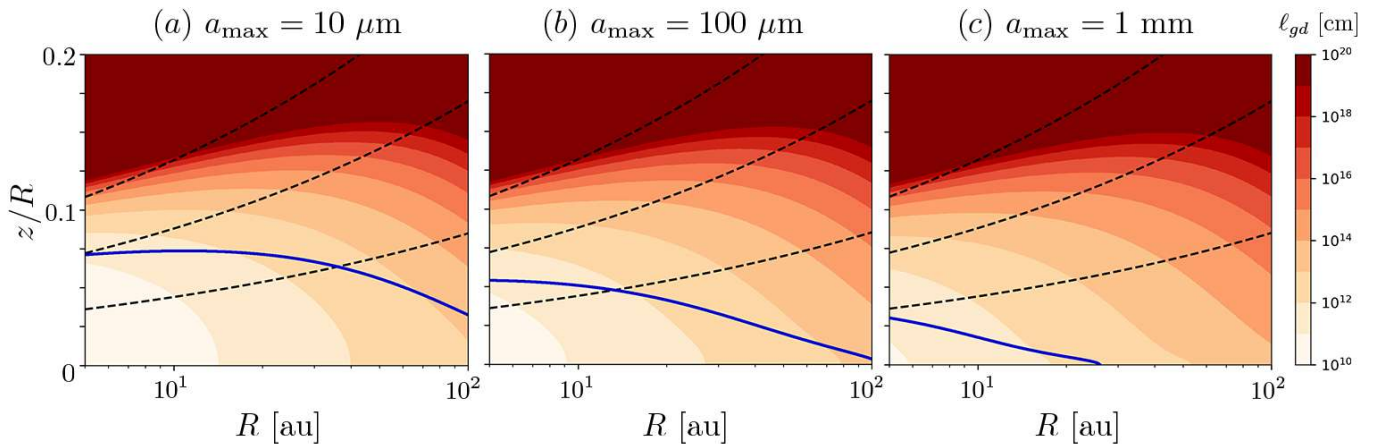


Figure 6. Mean travel length of gas molecules before colliding with dust particles, ℓ_{gd} , as a function of R and z/R for different values of a_{\max} with $\alpha_D = 10^{-4}$. The dashed lines represent H_g , $2H_g$, and $3H_g$ in height from the midplane. The solid lines correspond to the boundary of the VSI zone.

($L \approx 0.9H_g$). In the range of $k_x \leq k_{x,\max}$ and $|k_z| \geq |k_{z,\min}|$, Γ_{VSI} reaches a maximum of $0.003\Omega_K$ at $k_x = k_{x,\max}$ and $|k_z| = |k_{z,\min}|$ (marked by the star point in Figure 7). If we did not limit k_x and $|k_z|$, a higher maximum growth rate of $0.015\Omega_K$ would be reached at the point $k_x \approx 100/H_g$ and $|k_z| \approx 1.5/H_g$ ($L \approx H_g$) marked by the filled circle in Figure 7.

Figure 8 shows the wavenumbers of the most unstable VSI modes, $k_{x,\max}$ and $|k_{z,\min}|$, as a function of R for various values of α_D and a_{\max} . Note that $k_{x,\max}$ depends only on α_D whereas $|k_{z,\min}|$ depends on both α_D and a_{\max} . Being inversely proportional to the VSI zone vertical thickness L , $|k_{z,\min}|$ increases as a_{\max} increases or α_D decreases. Our assumption $|k_z| \ll k_x$ breaks down near the outer edge of the VSI zone where $|k_{z,\min}|$ diverges. However, this region is narrow compared to the VSI zone itself.

Figure 9 shows the maximum VSI growth rate $\Gamma_{\text{VSI,max}}$ as a function of R for various values of α_D and a_{\max} . Overall, $\Gamma_{\text{VSI,max}}$ decreases with increasing a_{\max} , reflecting the fact that the VSI zone shrinks as a_{\max} increases. In this default

disk model of $M_{\text{disk}} = 0.01M_\odot$, an increase in a_{\max} from $10 \mu\text{m}$ to $100 \mu\text{m}$ causes a decrease in $\Gamma_{\text{VSI,max}}$ by a factor of more than 10 at all $R \gtrsim 5 \text{ au}$, and increasing a_{\max} to 1 mm completely stabilizes the VSI at $R > 10 \text{ au}$ (but see Section 4.3 for the dependence on the disk mass). The maximum growth rate decreases mainly because the vertical shear $\partial(R\Omega)/\partial z$ at the top of the VSI zone, where we evaluate $\Gamma_{\text{VSI,max}}$, decreases as the VSI zone shrinks vertically (see Figure 1(c)). Decreasing α_D also causes a decrease in $\Gamma_{\text{VSI,max}}$, but this effect is minor compared to the effect of varying a_{\max} . Furthermore, decreasing α_D broadens the range of k_x to the short wavelength side (see Equation (23)) and promotes instability. However, this effect plays a minor role in the variation of $\Gamma_{\text{VSI,max}}$ with α_D .

Since our dispersion relation assumes zero viscosity and infinitesimally short cooling times, it is likely to underestimate the growth rates of modes with $k_x \sim k_{x,\max}$ and $|k_z| \sim |k_{z,\min}|$, respectively. Because the most unstable modes in our analysis have both $k_x = k_{x,\max}$ and $|k_z| = |k_{z,\min}|$, the

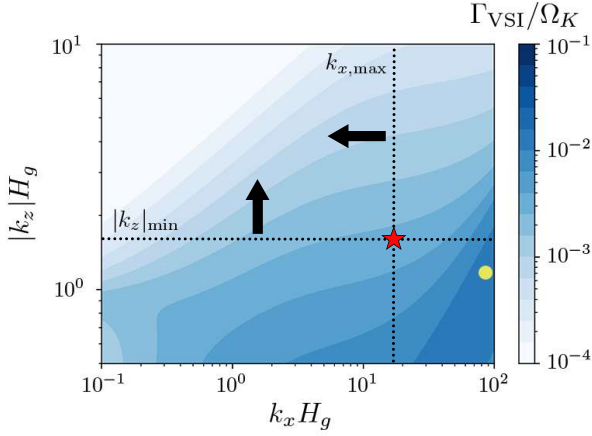


Figure 7. VSI growth rate Γ_{VSI} as a function of k_x and $|k_z|$ at the top of the VSI zone at $R = 60$ au for $a_{\text{max}} = 10 \mu\text{m}$ and $\alpha_D = 10^{-4}$. The vertical and horizontal dotted lines indicate $k_x = k_{x,\text{max}}$ and $k_z = |k_z|_{\text{min}}$, respectively. The star symbol marks the most unstable VSI mode in the range $k_x < k_{x,\text{max}}$ and $|k_z| > |k_z|_{\text{min}}$, which is limited by viscous damping and the finite vertical extent of the VSI zone. For comparison, the filled circle marks the mode that would be most unstable if the ranges of k_x and k_z were not limited.

maximum growth rate of the VSI predicted from our analysis should be regarded as an upper limit.

4.3. Variation of the VSI Zone Size with the Dust-to-Gas Ratio and Disk Mass

So far we have fixed the dust-to-gas mass ratio and disk mass to $\Sigma_d/\Sigma_g = 0.01$ and $M_{\text{disk}} = 0.01M_\odot$. The dust-to-gas ratio can decrease with time as dust particles tend to drift toward the central star owing to disk gas drag (Brauer et al. 2008). The disk mass can also depend on disk age; in particular, very young disks like the one around HL Tau can be as massive as $M_{\text{disk}} \sim 0.1M_\odot$ (Kwon et al. 2015). As highlighted in Section 4.1, the size of the VSI zone is controlled by ℓ_{gd} , with larger ℓ_{gd} leading to smaller VSI zones. Because $\ell_{\text{gd}}(z=0) \propto \Sigma_g^{1/2}/\Sigma_d \propto (\Sigma_d/\Sigma_g)^{-1}M_{\text{disk}}^{-1/2}$ (see Equation (36)), the VSI zone shrinks and expands as Σ_d/Σ_g decreases and M_{disk} increases, respectively.

We illustrate this in Figure 10, where we show the maps of the VSI zone for a disk with a lower dust-to-gas ratio of $\Sigma_d/\Sigma_g = 0.001$ and for a disk with a higher disk mass of $M_{\text{disk}} = 0.1 M_\odot$ (panels (b) and (c), respectively), both with $a_{\text{max}} = 1$ mm and $\alpha_D = 10^{-4}$. We find that the VSI zone is completely removed from $R > 5$ au for $\Sigma_d/\Sigma_g = 0.001$, whereas it extends out to 100 au for $M_{\text{disk}} = 0.1M_\odot$ even with $a_{\text{max}} = 1$ mm. The radial extent of the VSI zone for the latter case is almost the same as that for $M_{\text{disk}} = 0.01M_\odot$ and $a_{\text{max}} = 10 \mu\text{m}$ (see Figure 5(a)), consistent with the scaling $\ell_{\text{gd}}(z=0) \propto a_{\text{max}}^{1/2}(\Sigma_d/\Sigma_g)^{-1}M_{\text{disk}}^{-1/2}$ from Equation (36).

5. DISCUSSION

5.1. Correspondence between Vertically Local and Global Analyses

As mentioned in Section 3, we have employed the vertically local approximation to treat the modes within a VSI zone. For vertically wide ($L \sim H_g$) VSI zones, our local modes should correspond to some modes in the vertically global linear analysis.

Below, we show that the modes with the longest vertical wavelength ($|k_z| = |k_z|_{\text{min}}$, Equation (24)) indeed correspond to the fundamental corrugation modes in the global analysis. The fundamental corrugation modes are the modes with uniform vertical motion and are known to dominate the non-linear phase of the VSI (Nelson et al. 2013). In the limit of short cooling times, the vertically global dispersion relation for the fundamental corrugation modes can be written as (Lin & Youdin 2015)

$$\omega^2 = \frac{1 + ihq\hat{k}_x}{1 + \hat{k}_x^2} \Omega_K^2, \quad (37)$$

where $h = H_g/R$ and $\hat{k}_x = k_x H_g$. To show the correspondence between these vertically uniform modes and our local VSI modes with $|k_z| = |k_z|_{\text{min}}$, we focus on local inertial modes and neglect the ω^4 in our local dispersion relation (Equation (10)). We also use $\partial v_{y0}/\partial z \sim (qH_g/R)\Omega_K$, $N_z \ll \kappa_0 \approx \Omega_K$, $g \sim \Omega_K^2 H_g$, and $k_z = -|k_z|_{\text{min}} \sim -1/H_g$ for $L \sim H_g$. Our dispersion relation then reduces to

$$\omega^2 \sim \frac{1 - 2\hat{k}_x|q|h + ihq\hat{k}_x}{2 + \hat{k}_x^2} \Omega_K^2, \quad (38)$$

Since $\hat{k}_x|q|h \leq \hat{k}_{x,\text{max}}|q|h \lesssim 1$ for $\alpha_D \gtrsim 10^{-5}$ (see Equation (23)), Equation (38) agrees with Equation (37) to within a factor of order unity. Because the most unstable modes in our analysis have $|k_z| = |k_z|_{\text{min}}$, our $\Gamma_{\text{VSI,max}}$ serves as a good estimate for the growth rate of the fundamental corrugation modes when $L \sim H_g$.

5.2. Can VSI-driven Turbulence Stably Sustain Vertical Dust Distribution?

The main limitation of our model is that it has to assume the strength of disk turbulence to calculate the vertical dust distribution. In reality, in outer disk regions where ambipolar diffusion suppresses MRI, the VSI itself can be the dominant source of disk turbulence. If this is the case, our model effectively assumes that the strength of vertical diffusion caused by VSI-driven turbulence matches the diffusion strength α_D required to sustain the vertical dust distribution. The system would evolve until two diffusion coefficients match, but we cannot tell if such equilibrium states would exist because our current model relying on linear stability analysis does not predict the strength of VSI-driven turbulence.

Moreover, even if there exists an equilibrium state, the state can be unstable against perturbations to the vertical

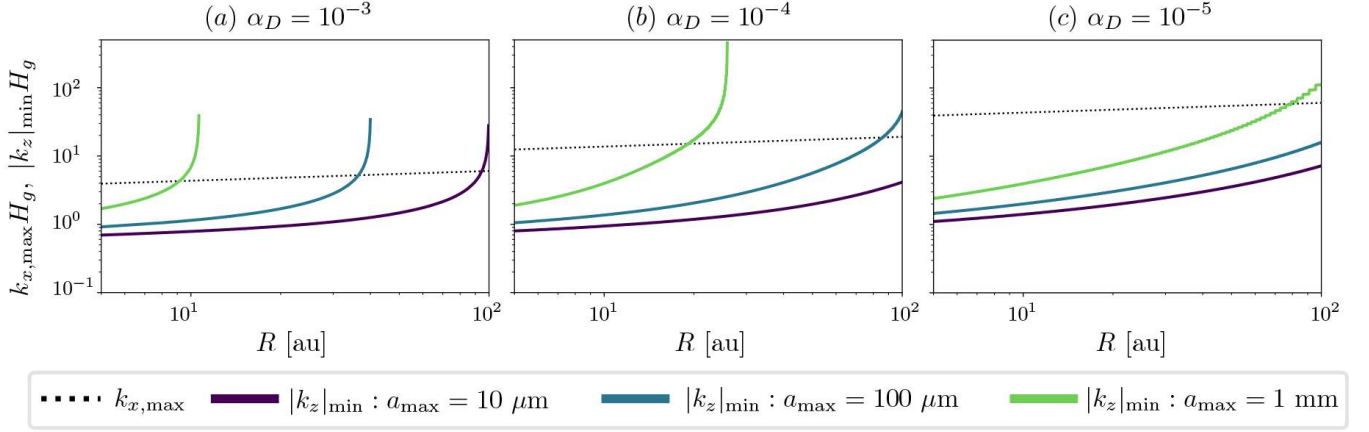


Figure 8. Maximum radial wavenumber $k_{x,\max}$ (dotted lines; Equation (23)) and minimum vertical wavenumber $|k_z|_{\min}$ (solid lines; Equation (24)) as a function R for different values of α_D and a_{\max} . These are equal to the wavenumbers of the most unstable VSI mode (see Section 4.2).

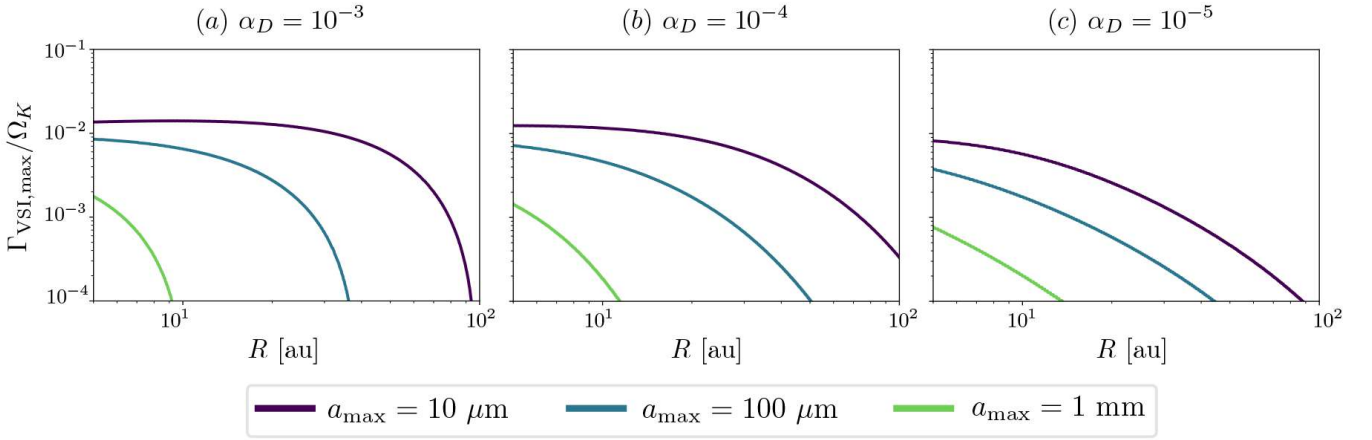


Figure 9. Maximum VSI growth rate $\Gamma_{\text{VSI,max}}$ as a function of R for different values of α_D with $a_{\max} = 10 \mu\text{m}$, $100 \mu\text{m}$, and 1mm .

dust distribution. Unstable equilibrium is expected if, for instance, a small decrease in the dust scale height causes a large decrease in the VSI turbulence strength, in which case dust settling would proceed in a runaway fashion. Dust settling also introduces effective vertical buoyancy that further stabilizes the VSI in the settled dust layers (Lin 2019; Schäfer et al. 2020). The stability of the system should be studied in future hydrodynamical simulations that include both the thermal and frictional coupling between the gas and dust.

5.3. Implications for Dust Growth, Settling, and Planetesimal Formation in Outer Disk Regions

We have shown that dust growth can substantially suppress the VSI beyond 10 au. This suggests that disk turbulence in this outer disk region would become weaker as dust grows. This may provide positive feedback to dust growth and also planetesimal formation. Weaker turbulence would suppress collisional fragmentation of the dust particles and thereby further promote dust growth (e.g., Brauer et al. 2008;

Birnstiel et al. 2010; Okuzumi & Hirose 2012). Weak turbulence are also preferred for planetesimal formation via the streaming and gravitational instabilities, both of which require substantial dust settling toward the midplane (Sekiya 1998; Youdin & Shu 2002; Johansen et al. 2009). These positive feedback effects are potentially important for understanding planet formation and dust ring/gap formation in outer regions of protoplanetary disks.

Suppression of the VSI at large radial distances due to dust growth may also explain the high degree of dust settling in the HL Tau disk (Pinte et al. 2016). However, quantitative estimates for the strength of VSI-driven turbulence are needed to test this hypothesis because, as we have seen in Section 4.3, the VSI tends to be vigorous in massive disks like the HL Tau disk ($M_{\text{disk}} \sim 0.1 M_{\odot}$; Kwon et al. 2015). Very recently, Doi & Kataoka (2021) measured the vertical thicknesses of two dust rings at 70 and 100 au in the massive disk around HD 163296, and showed that the outer ring is

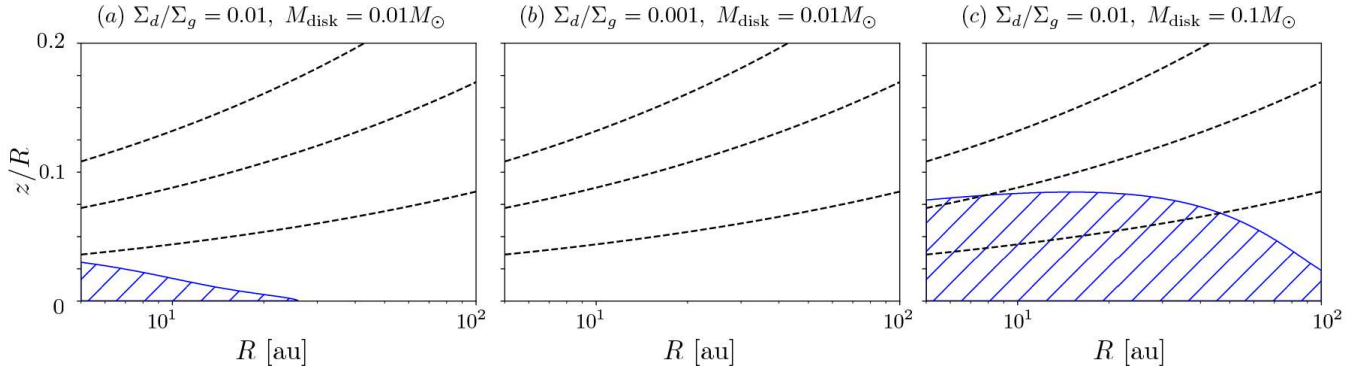


Figure 10. Location of the VSI zone (shaded area) for different values of Σ_d/Σ_g and M_{disk} with $a_{\text{max}} = 1 \text{ mm}$ and $\alpha_D = 10^{-4}$. The dashed lines represent H_g , $2H_g$, and $3H_g$ in height from the midplane.

much thinner than the gas disk but the inner ring is as thick as the gas disk. This may suggest that the VSI is active at $\sim 70 \text{ au}$ in this disk (see Bi et al. 2021 and Binkert et al. 2021 for another potential interpretation). We plan to address these open issues in future work.

6. CONCLUSIONS

We have investigated the impacts of dust growth and settling on the VSI in the outer regions of protoplanetary disks using a model based on linear stability analysis. Our key findings are summarized as follows.

1. For fixed dust particle size distribution, a higher degree of dust settling (corresponding to a lower value of turbulence strength α_D) leads to a VSI zone that is more confined to the midplane and more extended to larger radial distances (Figure 3). This is because in outer disk regions of low optical depths, dust settling causes a decrease and an increase in the timescale of thermal conduction from gas to dust ($\propto \ell_{\text{gd}}$; Equation (19)) at the midplane and well above the midplane, respectively (Figure 4).
2. For fixed turbulence strength, the VSI zone shrinks toward the midplane and also toward the central star as dust particles grow (Figure 5). Dust growth also causes dust settling, but the decrease in the total surface area of the particles due to dust growth dominates the change in the thermal relaxation timescale (Figure 6).

3. The maximum growth rate of the VSI decreases as dust particles grow. In our default disk model assuming $M_{\text{disk}} = 0.01 M_{\odot}$, dust growth to 1 mm in size completely stabilizes the VSI exterior to 10 au (Figure 9). On the other hand, the VSI is more vigorous in disks with larger disk masses (Section 4.3).

Our results suggest that dust evolution, in particular dust growth, should lead to suppression of VSI-driven turbulence. This effect may enable further dust coagulation and settling and may potentially promote planetesimal formation in outer disk regions. The effect may also explain the high degree of dust settling observed in the dust rings around HL Tau, but testing this hypothesis requires more qualitative investigation of the interplay between dust evolution and the nonlinear development of the VSI.

ACKNOWLEDGMENTS

We thank Shoji Mori for the discussions that motivated this project. We also thank the referee for a helpful report that motivated us to discuss the correspondence between local and global linear analyses. This work was supported by JSPS KAKENHI Grant Numbers JP20H01948, JP20H00182, JP19K03926, JP18H05438 and JP20J01376.

REFERENCES

- Adachi, I., Hayashi, C., & Nakazawa, K. 1976, Progress of Theoretical Physics, 56, 1756, doi: [10.1143/PTP.56.1756](https://doi.org/10.1143/PTP.56.1756)
- ALMA Partnership, Brogan, C. L., Pérez, L. M., et al. 2015, ApJL, 808, L3, doi: [10.1088/2041-8205/808/1/L3](https://doi.org/10.1088/2041-8205/808/1/L3)
- Andrews, S. M. 2020, ARA&A, 58, 483, doi: [10.1146/annurev-astro-031220-010302](https://doi.org/10.1146/annurev-astro-031220-010302)
- Andrews, S. M., Huang, J., Pérez, L. M., et al. 2018, ApJL, 869, L41, doi: [10.3847/2041-8213/aaf741](https://doi.org/10.3847/2041-8213/aaf741)
- Arlt, R., & Urpin, V. 2004, A&A, 426, 755, doi: [10.1051/0004-6361:20035896](https://doi.org/10.1051/0004-6361:20035896)
- Bai, X.-N. 2015, ApJ, 798, 84, doi: [10.1088/0004-637X/798/2/84](https://doi.org/10.1088/0004-637X/798/2/84)

- Balbus, S. A., & Hawley, J. F. 1991, *ApJ*, 376, 214, doi: [10.1086/170270](https://doi.org/10.1086/170270)
- Barker, A. J., & Latter, H. N. 2015, *MNRAS*, 450, 21, doi: [10.1093/mnras/stv640](https://doi.org/10.1093/mnras/stv640)
- Bi, J., Lin, M.-K., & Dong, R. 2021, arXiv e-prints, arXiv:2103.09254. <https://arxiv.org/abs/2103.09254>
- Binkert, F., Szulágyi, J., & Birnstiel, T. 2021, arXiv e-prints, arXiv:2103.10177. <https://arxiv.org/abs/2103.10177>
- Birnstiel, T., Dullemond, C. P., & Brauer, F. 2010, *A&A*, 513, A79, doi: [10.1051/0004-6361/200913731](https://doi.org/10.1051/0004-6361/200913731)
- Birnstiel, T., Ormel, C. W., & Dullemond, C. P. 2011, *A&A*, 525, A11, doi: [10.1051/0004-6361/201015228](https://doi.org/10.1051/0004-6361/201015228)
- Bitsch, B., Johansen, A., Lambrechts, M., & Morbidelli, A. 2015, *A&A*, 575, A28, doi: [10.1051/0004-6361/201424964](https://doi.org/10.1051/0004-6361/201424964)
- Bohren, C. F., & Huffman, D. R. 1983, *Absorption and scattering of light by small particles*
- Brauer, F., Dullemond, C. P., & Henning, T. 2008, *A&A*, 480, 859, doi: [10.1051/0004-6361:20077759](https://doi.org/10.1051/0004-6361:20077759)
- Carrera, D., Johansen, A., & Davies, M. B. 2015, *A&A*, 579, A43, doi: [10.1051/0004-6361/201425120](https://doi.org/10.1051/0004-6361/201425120)
- Chiang, E. I., & Goldreich, P. 1997, *ApJ*, 490, 368, doi: [10.1086/304869](https://doi.org/10.1086/304869)
- Chokshi, A., Tielens, A. G. G. M., & Hollenbach, D. 1993, *ApJ*, 407, 806, doi: [10.1086/172562](https://doi.org/10.1086/172562)
- Cui, C., & Bai, X.-N. 2020, *ApJ*, 891, 30, doi: [10.3847/1538-4357/ab7194](https://doi.org/10.3847/1538-4357/ab7194)
- Doi, K., & Kataoka, A. 2021, arXiv e-prints, arXiv:2102.06209. <https://arxiv.org/abs/2102.06209>
- Dominik, C., & Tielens, A. G. G. M. 1997, *ApJ*, 480, 647, doi: [10.1086/303996](https://doi.org/10.1086/303996)
- Dubrulle, B., Morfill, G., & Sterzik, M. 1995, *Icarus*, 114, 237, doi: [10.1006/icar.1995.1058](https://doi.org/10.1006/icar.1995.1058)
- Flaherty, K., Hughes, A. M., Simon, J. B., et al. 2020, *ApJ*, 895, 109, doi: [10.3847/1538-4357/ab8cc5](https://doi.org/10.3847/1538-4357/ab8cc5)
- Flaherty, K. M., Hughes, A. M., Rosenfeld, K. A., et al. 2015, *ApJ*, 813, 99, doi: [10.1088/0004-637X/813/2/99](https://doi.org/10.1088/0004-637X/813/2/99)
- Flaherty, K. M., Hughes, A. M., Teague, R., et al. 2018, *ApJ*, 856, 117, doi: [10.3847/1538-4357/aab615](https://doi.org/10.3847/1538-4357/aab615)
- Flaherty, K. M., Hughes, A. M., Rose, S. C., et al. 2017, *ApJ*, 843, 150, doi: [10.3847/1538-4357/aa79f9](https://doi.org/10.3847/1538-4357/aa79f9)
- Flock, M., Nelson, R. P., Turner, N. J., et al. 2017, *ApJ*, 850, 131, doi: [10.3847/1538-4357/aa943f](https://doi.org/10.3847/1538-4357/aa943f)
- Flock, M., Turner, N. J., Nelson, R. P., et al. 2020, *ApJ*, 897, 155, doi: [10.3847/1538-4357/ab9641](https://doi.org/10.3847/1538-4357/ab9641)
- Fricke, K. 1968, *ZA*, 68, 317
- Goldreich, P., & Schubert, G. 1967, *ApJ*, 150, 571, doi: [10.1086/149360](https://doi.org/10.1086/149360)
- Goldreich, P., & Ward, W. R. 1973, *ApJ*, 183, 1051, doi: [10.1086/152291](https://doi.org/10.1086/152291)
- Hartmann, L., Calvet, N., Gullbring, E., & D'Alessio, P. 1998, *ApJ*, 495, 385, doi: [10.1086/305277](https://doi.org/10.1086/305277)
- Johansen, A., & Youdin, A. 2007, *ApJ*, 662, 627, doi: [10.1086/516730](https://doi.org/10.1086/516730)
- Johansen, A., Youdin, A., & Mac Low, M.-M. 2009, *ApJL*, 704, L75, doi: [10.1088/0004-637X/704/2/L75](https://doi.org/10.1088/0004-637X/704/2/L75)
- Kataoka, A., Tanaka, H., Okuzumi, S., & Wada, K. 2013, *A&A*, 557, L4, doi: [10.1051/0004-6361/201322151](https://doi.org/10.1051/0004-6361/201322151)
- Kwon, W., Looney, L. W., Mundy, L. G., & Welch, W. J. 2015, *ApJ*, 808, 102, doi: [10.1088/0004-637X/808/1/102](https://doi.org/10.1088/0004-637X/808/1/102)
- Latter, H. N., & Papaloizou, J. 2018, *MNRAS*, 474, 3110, doi: [10.1093/mnras/stx3031](https://doi.org/10.1093/mnras/stx3031)
- Lin, M.-K. 2019, *MNRAS*, 485, 5221, doi: [10.1093/mnras/stz701](https://doi.org/10.1093/mnras/stz701)
- Lin, M.-K., & Youdin, A. N. 2015, *ApJ*, 811, 17, doi: [10.1088/0004-637X/811/1/17](https://doi.org/10.1088/0004-637X/811/1/17)
- . 2017, *ApJ*, 849, 129, doi: [10.3847/1538-4357/aa92cd](https://doi.org/10.3847/1538-4357/aa92cd)
- Long, F., Pinilla, P., Herczeg, G. J., et al. 2018, *ApJ*, 869, 17, doi: [10.3847/1538-4357/aae8e1](https://doi.org/10.3847/1538-4357/aae8e1)
- Lynden-Bell, D., & Pringle, J. E. 1974, *MNRAS*, 168, 603, doi: [10.1093/mnras/168.3.603](https://doi.org/10.1093/mnras/168.3.603)
- Lyra, W., & Umurhan, O. M. 2019, *PASP*, 131, 072001, doi: [10.1088/1538-3873/aaf5ff](https://doi.org/10.1088/1538-3873/aaf5ff)
- Malygin, M. G., Klahr, H., Semenov, D., Henning, T., & Dullemond, C. P. 2017, *A&A*, 605, A30, doi: [10.1051/0004-6361/201629933](https://doi.org/10.1051/0004-6361/201629933)
- Mathis, J. S., Rumpl, W., & Nordsieck, K. H. 1977, *ApJ*, 217, 425, doi: [10.1086/155591](https://doi.org/10.1086/155591)
- Nelson, R. P., Gressel, O., & Umurhan, O. M. 2013, *MNRAS*, 435, 2610, doi: [10.1093/mnras/stt1475](https://doi.org/10.1093/mnras/stt1475)
- . 2016, *MNRAS*, 456, 239, doi: [10.1093/mnras/stv2440](https://doi.org/10.1093/mnras/stv2440)
- Okuzumi, S., & Hirose, S. 2012, *ApJL*, 753, L8, doi: [10.1088/2041-8205/753/1/L8](https://doi.org/10.1088/2041-8205/753/1/L8)
- Okuzumi, S., Tanaka, H., Kobayashi, H., & Wada, K. 2012, *ApJ*, 752, 106, doi: [10.1088/0004-637X/752/2/106](https://doi.org/10.1088/0004-637X/752/2/106)
- Pfeil, T., & Klahr, H. 2019, *ApJ*, 871, 150, doi: [10.3847/1538-4357/aaf962](https://doi.org/10.3847/1538-4357/aaf962)
- Pierens, A. 2021, *MNRAS*, doi: [10.1093/mnras/stab183](https://doi.org/10.1093/mnras/stab183)
- Pinte, C., Dent, W. R. F., Ménard, F., et al. 2016, *ApJ*, 816, 25, doi: [10.3847/0004-637X/816/1/25](https://doi.org/10.3847/0004-637X/816/1/25)
- Riols, A., & Lesur, G. 2018, *A&A*, 617, A117, doi: [10.1051/0004-6361/201833212](https://doi.org/10.1051/0004-6361/201833212)
- Schäfer, U., Johansen, A., & Banerjee, R. 2020, *A&A*, 635, A190, doi: [10.1051/0004-6361/201937371](https://doi.org/10.1051/0004-6361/201937371)
- Sekiya, M. 1998, *Icarus*, 133, 298, doi: [10.1006/icar.1998.5933](https://doi.org/10.1006/icar.1998.5933)
- Simon, J. B., Bai, X.-N., Armitage, P. J., Stone, J. M., & Beckwith, K. 2013a, *ApJ*, 775, 73, doi: [10.1088/0004-637X/775/1/73](https://doi.org/10.1088/0004-637X/775/1/73)
- Simon, J. B., Bai, X.-N., Stone, J. M., Armitage, P. J., & Beckwith, K. 2013b, *ApJ*, 764, 66, doi: [10.1088/0004-637X/764/1/66](https://doi.org/10.1088/0004-637X/764/1/66)
- Stoll, M. H. R., & Kley, W. 2014, *A&A*, 572, A77, doi: [10.1051/0004-6361/201424114](https://doi.org/10.1051/0004-6361/201424114)

- Takahashi, S. Z., & Inutsuka, S.-i. 2014, *ApJ*, 794, 55, doi: [10.1088/0004-637X/794/1/55](https://doi.org/10.1088/0004-637X/794/1/55)
- Takeuchi, T., & Lin, D. N. C. 2002, *ApJ*, 581, 1344, doi: [10.1086/344437](https://doi.org/10.1086/344437)
- Tominaga, R. T., Inutsuka, S.-i., & Takahashi, S. Z. 2018, *PASJ*, 70, 3, doi: [10.1093/pasj/psx143](https://doi.org/10.1093/pasj/psx143)
- Tominaga, R. T., Takahashi, S. Z., & Inutsuka, S.-i. 2019, *ApJ*, 881, 53, doi: [10.3847/1538-4357/ab25ea](https://doi.org/10.3847/1538-4357/ab25ea)
- . 2020, *ApJ*, 900, 182, doi: [10.3847/1538-4357/abad36](https://doi.org/10.3847/1538-4357/abad36)
- Urpin, V. 2003, *A&A*, 404, 397, doi: [10.1051/0004-6361:20030513](https://doi.org/10.1051/0004-6361:20030513)
- Urpin, V., & Brandenburg, A. 1998, *MNRAS*, 294, 399, doi: [10.1046/j.1365-8711.1998.01118.x](https://doi.org/10.1046/j.1365-8711.1998.01118.x)
- van der Marel, N., Dong, R., di Francesco, J., Williams, J. P., & Tobin, J. 2019, *ApJ*, 872, 112, doi: [10.3847/1538-4357/aafd31](https://doi.org/10.3847/1538-4357/aafd31)
- Weidenschilling, S. J. 1977, *MNRAS*, 180, 57, doi: [10.1093/mnras/180.2.57](https://doi.org/10.1093/mnras/180.2.57)
- Whipple, F. L. 1972, in *From Plasma to Planet*, ed. A. Elvius, 211
- Windmark, F., Birnstiel, T., Ormel, C. W., & Dullemond, C. P. 2012, *A&A*, 544, L16, doi: [10.1051/0004-6361/201220004](https://doi.org/10.1051/0004-6361/201220004)
- Yang, C. C., Johansen, A., & Carrera, D. 2017, *A&A*, 606, A80, doi: [10.1051/0004-6361/201630106](https://doi.org/10.1051/0004-6361/201630106)
- Youdin, A. N. 2011, *ApJ*, 731, 99, doi: [10.1088/0004-637X/731/2/99](https://doi.org/10.1088/0004-637X/731/2/99)
- Youdin, A. N., & Goodman, J. 2005, *ApJ*, 620, 459, doi: [10.1086/426895](https://doi.org/10.1086/426895)
- Youdin, A. N., & Lithwick, Y. 2007, *Icarus*, 192, 588, doi: [10.1016/j.icarus.2007.07.012](https://doi.org/10.1016/j.icarus.2007.07.012)
- Youdin, A. N., & Shu, F. H. 2002, *ApJ*, 580, 494, doi: [10.1086/343109](https://doi.org/10.1086/343109)

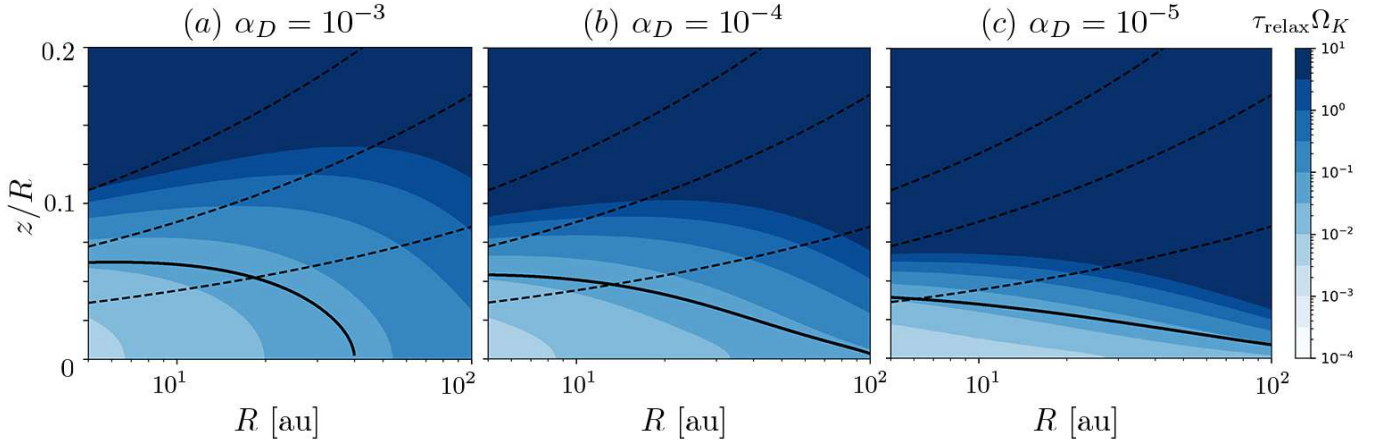


Figure 11. Thermal relaxation timescale τ_{relax} normalized by Ω_K^{-1} as a function of R and z/R for different values of α_D with $a_{\text{max}} = 100 \mu\text{m}$. The dashed lines represent $z = H_g, 2H_g,$ and $3H_g$. The solid line marks $\tau_{\text{relax}} = \tau_{\text{crit}}$.

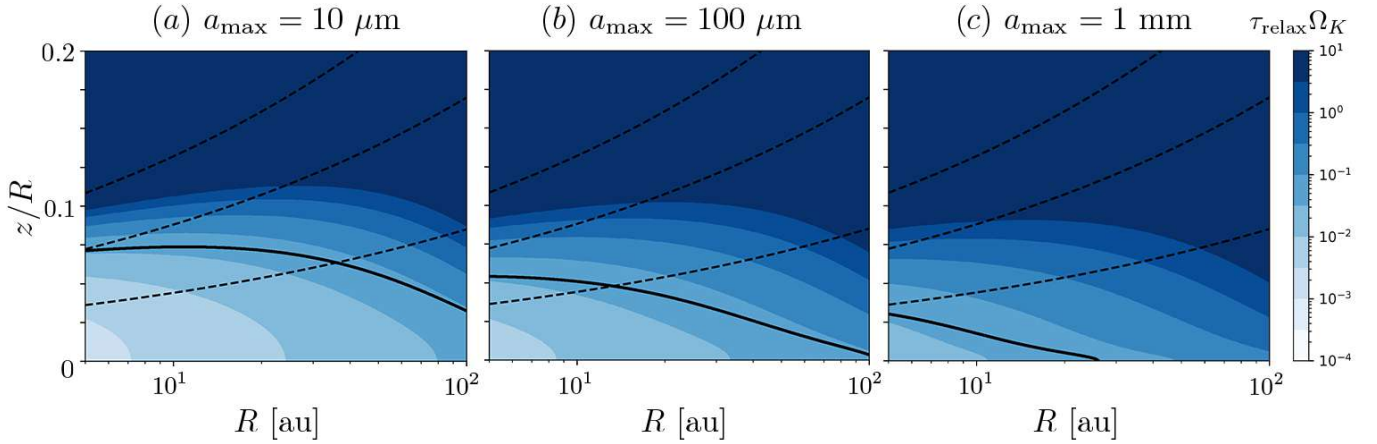


Figure 12. Thermal relaxation timescale τ_{relax} normalized by Ω_K^{-1} as a function of R and z/R for different values of a_{max} with $\alpha_D = 10^{-4}$. The dashed lines represent $z = H_g, 2H_g,$ and $3H_g$. The solid line marks $\tau_{\text{relax}} = \tau_{\text{crit}}$.

APPENDIX

A. THERMAL RELAXATION TIMESCALE

Figures 11 and Figure 12 show τ_{relax} ($= \tau_{\text{coll}}$) normalized by Ω_K^{-1} as a function of R and z for all parameter sets considered in this study. A smaller α_D produces a larger τ_{relax} well above the midplane (because $\tau_{\text{relax}} = \tau_{\text{coll}} \propto \ell_{\text{gd}}$; see Figure 4), resulting in a VSI zone that is more confined to the midplane (see the boundaries of the VSI zones marked by the solid lines in Figure 11). A larger a_{max} causes an increase in τ_{relax} at all heights and hence leads to a narrower VSI zone.